Dual delivery of IL-10 and AT-RvD1 from PEG hydrogels polarize immune cells towards pro-regenerative phenotypes

Mary Caitlin P. Sok[a,c,1], **Nusaiba Baker**[a,c,1], **Claire McClain**[a], **Hong Seo Lim**[a], **Thomas Turner**[a], **Lauren Hymel**[a], **Molly Ogle**[a], **Claire Olingy**[a], **Joshua I. Palacios**[a], **José R. Garcia**[a], **Krithik Srithar**[a], **Andrés J. García**[b,d], **Peng Qiu**[a,b], **Edward A. Botchwey**[a,b,*]

[a]Wallace H. Coulter Department of Biomedical Engineering at Georgia Institute of Technology and Emory University, Atlanta, GA, USA

[b]Parker H. Petit Institute for Bioengineering and Bioscience, Georgia Institute of Technology, Atlanta, GA, USA

[c]Emory University Medical Scientist Training Program, USA

[d]George W. Woodruff School of Mechanical Engineering, Georgia Institute of Technology, Atlanta, GA, USA

Abstract

Inflammation after traumatic injury or surgical intervention is both a protective tissue response leading to regeneration and a potential cause of wound complications. One potentially successful strategy to harness to pro- regenerative roles of host inflammation is the localized delivery of bioactive materials to induce immune suppressive cellular responses by cells responding to injury. In this study, we designed a fully synthetic poly (ethylene) glycol (PEG)-based hydrogel to release the specialized pro-resolving lipid mediator aspirin-triggered resolvin-D1 (AT-RvD1) and recombinant human interleukin 10 (IL-10). We utilized a unique side-by-side internally controlled implant design wherein bioactive hydrogels were implanted adjacent to control hydrogels devoid of immune modulatory factors in the dorsal skinfold window chamber. We also explored single-immune cell data with unsupervised approaches such as SPADE. First, we show that RGD-presenting hydrogel delivery results in enhanced immune cell recruitment to the site of injury. We then use intra-vital imaging to assess cellular recruitment and microvascular remodeling to show an increase in the caliber and density of local microvessels. Finally, we show that

the recruitment and re-education of mononuclear phagocytes by combined delivery IL-10 and AT-RvD1 localizes immune suppressive subsets to the hydrogel, including CD206^{+} macrophages (M2a/c) and IL-10 expressing dendritic cells in the context of chronic inflammation following surgical tissue disruption. These data demonstrate the potential of combined delivery on the recruitment of regenerative cell subsets involved in wound healing complications.

Keywords

Bioactive lipids; Inflammation resolution; Peripheral tolerance; Engineered hydrogels

1. Introduction

The immune response to injury is a complex process that involves the functional orchestration of many different cell populations that work in coordination to restore tissue homeostasis [1]. In healthy individuals or in the case of small wounds, tissue regeneration and the return to normal function proceed without any necessary outside intervention. However, in the case of aging, large wounds, or in disease states such as diabetes or after organ transplant, the process of the immune response to wound healing is dysregulated and may prevent normal tissue regeneration, leading to failure of wound closure or a chronic inflammatory state [2, 3]. In order to mitigate the immune dysregulation present during these states, there is a rapidly expanding body of research dedicated to the targeting and manipulation of the immune response to injury and inflammation. Studies have shown the roles of single immune populations during the process of tissue regulation. For example, depletion of neutrophils delays wound closure in aged mice, and clinical observations note that neutropenic individuals often have difficulty healing wounds [4,5]. Additionally, ablation of monocyte and macrophage pools in zebrafish and salamanders has resulted in failure of limb or tail regeneration, indicating their indispensability to the regenerative process [6,7]. These studies demonstrate the extensive crosstalk and interplay between cell types during wound healing – that no one cell is the master orchestrator of tissue regeneration. Thus, we aimed to develop a therapeutic to target multiple immune populations involved in inflammation and wound healing.

Within the monocyte and macrophage families, subsets have been identified in both mice and humans that have disparate functions and roles during inflammation. Monocytes may exist as classical inflammatory monocytes (CD11b+Ly6Chi in mice and CD14^{+}CD16^{−} in humans) that exhibit largely pro-inflammatory characteristics – or as patrolling non-classical anti-inflammatory monocytes (CD11b+ Ly6Clow in mice and CD14low CD16+ in humans) [8]. After injury they infiltrate into tissue and secrete various bioactive factors including vascular endothelial growth factor (VEGF), transforming growth factor beta (TGF-β), and interleukin-10 (IL-10) to promote angiogenesis and matrix deposition [9–12]. We have shown that targeted recruitment of this specific monocyte subset enhances microvascular network expansion after sterile injury, and that they are able to preferentially expand the population of "anti-inflammatory" wound-healing macrophages [13–16]. By extension, macrophages exist *in vivo* on a spectrum from M1 "pro-inflammatory" to M2 "anti-inflammatory" [17]. M2 anti-inflammatory macrophages are identified by their expression

of canonical macrophage markers MerTK and CD64, and can also express high or low Ly6C [14,18,19]. These M2 macrophages can be further divided into M2a-c subsets, and the M2a (CD206+) and M2c (CD163+) subsets have, in particular, been shown to exhibit pro-regenerative, anti-inflammatory characteristics, such as the ability to release IL-10 and support angiogenesis [20–24].

In addition to the mononuclear phagocyte system, other cells in the innate and adaptive immune systems also positively influence regeneration. Dendritic cells (DCs) are antigen presenting cells that release cytokines and are responsible for influencing both innate and adaptive immune responses after microbial infection or tissue injury [25]. Traditionally, their function is to detect and capture foreign antigen and present those antigens to T lymphocytes to induce their activation, differentiation, and subsequent action [26]. Additionally, DCs are involved in promoting tolerance to self-antigens and can induce regulatory T cell (Treg) expansion under the correct conditions [27]. Thus, therapeutic strategies for promoting the anti-inflammatory roles of DCs aim to increase expression of inhibitory molecules and tolerogenic mediators [28, 29]. One strategy for modulating the local immune cell population after injury is through local delivery of biomolecules via implanted biomaterials. Although other groups have loaded bioactive hydrogels with various compounds such as black phosphorus to encourage angiogenesis and reduce inflammation to encourage healing [30], delivery of one single biomolecule to sufficiently modulate the recruitment of diverse immune cell subsets remains a significant challenge. Therefore, we have identified two bioactive factors capable of eliciting this response: aspirin-triggered resolvin D1 (AT-RvD1) and IL-10. AT-RvD1 is part of a class of "specialized pro-resolving mediators" (SPMs) capable of redirecting the immune response towards resolution [31]. SPMs have broad effects over a variety of myeloid cells, including the limitation of neutrophil transendothelial migration, the modulation of cytokine release from monocytes and macrophages, and the prevention of DC maturation [32–34]. We have previously shown that AT-RvD1 delivered from a PLGA film can increase local populations of Ly6Clow monocytes and CD206+ macrophages after injury [16] IL-10, a cytokine which plays a critical role in the control of immune responses, is also expressed by both innate and adaptive immune cells including monocytes, macrophages, dendritic cells, and T cell subsets [35]. IL-10 treatment promotes the transition from an M1 to M2 fate, and prevents DC maturation, resulting in decreased MHC-II surface receptor expression and subsequent increased release of IL-10 [36,37]. Additionally, IL-10 can act on T helper subsets to prevent their co-stimulation and proliferation [35]. Thiolated IL-10 has previously been conjugated to PEG-diacrylate UV-photocrosslinkable hydrogels and was shown to modulate *in* vitro dendritic cell activity [38]. These qualities of AT-RvD1 and IL-10 make an attractive combination therapy for the promotion of wound healing due to their synergistic ability to direct anti-inflammatory effector functions of lymphoid cell subsets.

Using the murine dorsal skinfold window chamber as a test bed to measure the response to immunomodulatory hydrogels, we demonstrate that not only is the recruitment of anti-inflammatory myeloid cells enhanced by AT-RvD1 delivery, but combination IL-10+AT-RvD1 treatment is able to concurrently increase populations of macrophages, dendritic cells, and T cells involved in wound healing. Unsupervised analysis strategies such as SPADE were used to highlight novel immune modulations following therapeutic hydrogel treatment.

These results indicate that an immunomodulatory strategy that coordinates activities of pro-regenerative/anti-inflammatory cells of both the innate and adaptive immune system is a promising method for enhanced tissue regeneration and healing.

2. Results

2.1. RGD-functionalization of PEG hydrogels supports enhanced migration of local myeloid cells

To explore the activity of myeloid cells towards engineered hydrogels, we delivered hydrogels based on 4-arm maleimide-functionalized macromer (PEG-4MAL) with 4.5% weight/volume for all hydrogel formulation as determined from previous work, functionalized with RGD adhesive peptide or the inactive scrambled peptide control RDG into the dorsal skinfold of mice that express GFP under the CX3CR1 promoter (CX3CR1$^{GFP/+}$) (Fig. 1A and B). Hydrogel functionalization with RGD creates a microenvironment that supports cell-material integration [39]. RGD (Fig. 1C) or RDG (Fig. 1D) functionalized PEG gels were implanted on the exposed dermal layer on day 1 after injury. At day 3, we performed intravital laser scanning confocal microscopy and acquired 25–30-min videos to visualize cells interacting with the hydrogel implants. We then classified cells by their shortest distance from the hydrogel surface over the course of the video and found more cells within 10 μm of RGD-functionalized hydrogel than RDG surfaces (not shown). Most cell migration tracks were within 30 μm of the hydrogel surface. We then tracked the mean and maximum velocity of CX3CR1+ cells around each hydrogel and found that the mean velocity was greater around RGD hydrogels compared to RDG hydrogels only if the cells were within 30 μm of the hydrogel surface (Fig. 1E). Cells were insensitive to RGD if they were at greater distances (30–50, 50 + μm). This indicates that on average, hydrogels functionalized with RGD, aid in cell adherence, therefore encouraging cell interactions with the hydrogel as compared to the control RDG-functionalized hydrogel. Additionally, it suggests that RGD-functionalized hydrogels increase the velocity of myeloid cells within their immediate vicinity.

2.2. PEG-4MAL hydrogels support loading and release of thiolated IL-10 and soluble AT-RvD1

To modulate the activity of immune cells recruited to RGD hydrogels, we aimed to deliver therapeutic factors, IL-10 and AT-RvD1, to the site of injury (Fig. 2A and B). First, we optimized the release of fluorescently tagged unmodified IL-10 from the PEG-4MAL hydrogel with the goal of slow, sustained release (Fig. 2C). After 24 h, the gels had released 227.40 ± 1.71 ng of the loaded IL-10, over 90% of the initial dose. By 5 days, 235 ± 1.73 ng total IL-10 was released from the gel, and only 22.39 ± 4.85 ng was recovered from the digested gel. To modify the release kinetics to provide a more sustained delivery of IL-10, we functionalized IL-10 to add free cysteines in order to allow interaction with the PEG-MAL macromer during gel polymerization, which would then result in a more gradual release as the gel degrades. We modified the protein with Traut's reagent (2-iminothiolane), a thioimidate compound that reacts with primary amines to form sulfhydryl groups. Using a molar excess of Traut's reagent (30:1), the concentration of thiol groups found on the IL-10 was 0.89 ± 0.98 μM or approximately 3 free cysteine groups per IL-10 molecule. When

thiolated-IL-10 was reacted with PEG-4MAL and polymerized into hydrogels, we found that thiolation greatly slowed the release kinetics. In contrast to the unmodified IL-10, hydrogels encapsulating thiolated IL-10 released 7.67 ± 2.76 ng (3%) after 30 min, 26.91 ± 2.91 ng (11%) at 2 h, 32.39 ± 2.67 ng (13%) at 6 h, and 42.03 ± 2.45 ng (17%) by 24 h. After 5 days, hydrogels with thiolated IL-10 resulted in a cumulative release of 73.28 ± 3.55 ng (29%) at 5 days, with 176.72 ± 5.42 ng (71%) remaining IL-10 recovered from the gel after digestion (Fig. 2D). We then incorporated AT- RvD1 through bulk-encapsulation in the protease cleavable gels. AT- RvD1 was released from the gels in a manner similar to that of the unmodified IL-10, with 87.66 ± 1.29 ng of the total loaded 100 ng dose released by 24 h. By day 5, only 4 more nanograms were released, and the total release was measured to be 91.24 ± 1.11 ng (Fig. 2E). Release from dual-loaded gels showed there was no effect of dual loading on either release profile (not shown).

IL-10 pretreatment of RAW264.7 macrophages prior to LPS stimulation has been previously shown to reduce TNF- α release [40]. To test the bioactivity of thiolated IL-10 released from PEG-4MAL gels, we employed similar *in vitro* assay of IL-10-mediated suppression of TNF-α release by LPS-stimulated RAW264.7 macrophages, and utilized intracellular cytokine staining and flow cytometric analysis to assess TNF-α levels in RAW264.7 macrophages (Fig. 2F). First, we compared unmodified-IL-10, thiolated-IL-10 (t-IL-10), and thiolated-IL-10 conjugated with PEG-4MAL (PEG-t-IL-10) and found that all three were able to significantly reduce TNF-α expression after treatment with LPS compared to vehicle control (Fig. 2G). We then compared thiolated-IL-10 to AT-RvD1 and co-treatment of AT-RvD1 and IL-10. Again, we observed a significant reduction in TNF-α expression across all groups after LPS treatment compared to control (Fig. 2H). Altogether, this characterization data indicates that thiolation with Traut's reagent is able to support the loading and release of IL-10 into PEG-MAL hydrogels while maintaining its bioactivity, and that dual-loaded hydrogels containing thiolated-IL-10 and AT-RvD1 have temporally independent release profiles. All subsequent experiments utilized thiolated-IL-10, and IL-10 in text and figures will refer to thiolated-IL-10.

We have previously shown that AT-RvD1 recruits a subset of proangiogenic neutrophils after injury [16]. Thus, we first aimed to test whether delivery of IL-10, AT-RvD1, or dual therapeutic treatment led to increased vascular length density and arteriolar diameter, two measures of vascular remodeling. We delivered IL-10 alone, AT-RvD1 alone, and combined IL-10 and AT-RvD1 hydrogels each into the rostral side of the dorsal skin using the dorsal skinfold window chamber model (DSWC), with unloaded hydrogel injected onto the caudal end, taking measurements at day 1, 3, and 7 (Fig. 3A). In order to track changes in the vasculature, we used longitudinal brightfield intravital microscopy in the dorsal skin vascular networks after implantation. We took images on post-operative days 3 and 7 and compared them to images from day 0 immediately following surgery. By day 7, there is a marked increase in vascular tortuosity and vascularity of the dorsal skin compared to day 0 in the AT-RvD1 and IL-10+AT-RvD1-treated skin (Fig. 3A). Furthermore, when we quantified the changes in vasculature, we saw significant increases in vascular length density in AT-RvD1 animals alone or combined with IL-10. We also observed significant increases in arteriolar diameter in the same groups (Fig. 3B and C). Notably, the IL-10+AT-RvD1 group had significantly increased the arteriolar diameter by day 7 over IL-10 alone. This

data suggests that IL-10/AT-RvD1-releasing hydrogels modulate vascular remodeling and expansion after implantation.

2.3.   Innate immune cell infiltration correlates with increased vasculature

Next, we characterized the immune cell subsets recruited to the injected hydrogels and to nearby emergent vasculature (CD31$^+$, gray) (Fig. 4A). We stained whole mount dorsal tissue for the pan-monocyte/macrophage marker CD68 and M2 marker CD206 and used Imaris to render and quantify the accumulation of M2 macrophages compared to the total monocyte and macrophage population over time. Representative 20x confocal images demonstrate the increase in the total CD68$^+$ population over time (Fig. 4B). Qualitatively, these images show increased CD68$^+$CD206+ cellular expression in the AT-RvD1 and IL-10+AT-RvD1 groups. We found that quantification of 3D renderings confirms the qualitative findings and shows a steady increase over time from day one to day seven in the accumulation of CD68$^+$ CD206+ macrophages following AT-RvD1-only or combination IL-10+AT-RvD1 treatment (Fig. 4C). Treatment with IL-10 only did not significantly increase the population of CD206+ macrophages over time.

Given the increasing knowledge of the roles immune system and plays in promoting wound healing and tissue regeneration, we quantified the temporal response of dendritic cells to immunomodulatory PEG-MAL hydrogels. Imaris renderings of dorsal tissue were used to measure CD11c and IL-10 co-expression levels (Fig. 4D). The number of CD11c + cells also co-expressing IL-10 was significantly higher after IL-10+AT- RvD1 treatment compared to control at all time points (Fig. 4E). At day 7, there were significantly more IL-10 expressing CD11c DCs following treatment with IL-10. AT-RvD1 treatment increased IL-10 DC populations compared to control, but not to the level of IL-10 or IL-10+AT- RvD1 treatments.

2.4.   Anti-inflammatory macrophages and dendritic cells accumulate after local hydrogel delivery

After profiling the recruitment of circulating immune cell subsets in response to hydrogels, we investigated changes in single-cell immune subpopulations using flow cytometry. We examined dynamic changes in macrophage recruitment to the hydrogel at days 1, 3, and 7 after tissue injury and implantation of PEG-4MAL hydrogels. M1 classically activated macrophages were characterized by their expression of the co- stimulatory molecule CD86 and did not express the mannose receptor CD206. We observed an increase in the M1 population at day 3 when they comprised on average 15% of the total macrophage population. The M1 population then decreased by day 7 and, with a significant reduction following AT-RvD1 or combination IL-10+AT-RvD1 treatment compared to control (Fig. 5A). Conversely, M2-like alternatively activated macrophages were characterized as CD86$^-$ CD206+. At day 1, these macrophages made up a higher proportion of the total macrophage population, possibly due to pre-existing populations of tissue resident macrophages that express CD206 [41]. We found large increases in the M2 macrophage population at day 1 in the AT-RvD1-treated and IL-10+AT-RvD1 treated animals compared to unloaded hydrogel control. At days 3 and 7, the average proportion of M2 macrophages had increased compared to the previous timepoint. We did not observe any change between IL-10 treated

dorsal tissue when compared to its respective control. At these time points, we did observe significant increases in the M2 population after AT-RvD1 and dual delivery of IL-10 and AT-RvD1 compared to control at days 3 and 7 (Fig. 5B). This accumulation of M2 macrophages occurred at a faster rate with dual delivery hydrogels, as the population of M2 macrophages was significantly increased in IL-10+AT-RvD1 treated animals compared to AT-RvD1-only delivery at day 3, indicating a modulation in recruitment or differentiation kinetics driven by co-delivery of these two factors.

In addition to changes in the macrophage populations, we observed significant increases in IL-10+ dendritic cells after one week across all groups and found that IL-10 + DCs were significantly increased in combination IL-10+AT-RvD1 treatment compared to IL-10 only and AT- RvD1 only treatments (Fig. 5C). Consistent with our hypothesis that IL-10 and AT-RvD1 delivery are able to reduce the activation of pro- inflammatory pathways, we also observed decreased intracellular TNF-α expression in CD11c + dendritic cells at day 3 in the IL-10 alone and IL-10+AT-RvD1 hydrogel treatment groups, and reduced TNF- α expression across all groups at day 7 (Fig. 5D).

Flow cytometry and IMARIS imaging identified increased populations of pro-regenerative innate immune cells, so to better elucidate cellular heterogeneity within these populations at day 7, we used SPADE, a dimensionality reduction technique that hierarchically clusters phenotypically similar cells into "nodes" [42]. Each SPADE node is made up of a unique profile of surface marker expression, from which we were able to identify the change in immune cell frequency in response to immunomodulatory hydrogel treatment. We created SPADE representations using CD11b + cells as indicative of myeloid cells, and then used MerTK + CD64+ markers to create a base SPADE dendrogram, or "tree", indicative of macrophages. By overlaying individual immune cell markers onto this base SPADE dendrogram, we were able to identify nodes that were specific for CD86+, which indicated an M1 phenotype (Fig. 6A), or CD206+, indicating an M2-like phenotype (Fig. 6B). For the M2 population, we further identified CD206+ nodes as either Ly6C + high or low or Ly6C-, as well as MHC-II+/−, to elucidate the cellular heterogeneity in that population. In order to characterize changes in immune cell frequency over pseudotime, a quantitative measure of biological processes, we assigned each node an immune phenotype and calculated the percent frequency of each cell population relative to the total number of events in each node. We then subtracted the percent cell frequency of each treatment group in each node from the cell frequency in the control group to create a "tornado plot", which indicate whether the abundance of that cell phenotype is dominated by control or treatment groups. This analysis shows that, in IL-10 and AT-RvD1 alone, when comparing the treatment group against the control, there does not seem to be a shift in M1 macrophage cell frequencies in any of the nodes. However, in the dual hydrogel group, there is a shift in cell frequency towards control groups in M1 macrophages (Fig. 6C). In M2 macrophage dominated nodes, there is a slight shift towards the treatment group, indicating the immune microenvironment transitioning towards a pro-regenerative phenotype by day 7 (Fig. 6D). This shift can be further characterized by Ly6Chi and low cells, with CD206+ Ly6Clo MHC-II + macrophage nodes dominated by the treatment groups, and CD206+ LyC- or LyChi nodes dominated by control groups.

We next created a CD11c + SPADE dendrogram to identify IL-10+ DCs (Fig. 7A). We identified 32 nodes that co-expressed markers CD11c+ and IL-10+. From the dendritic cell tree, we observed higher numbers of nodes dominated by IL-10+ DCs in all three treatment groups when compared to control (Fig. 7B). In particular, the IL-10+AT- RvD1 combined group was completely dominated by IL-10+ DC nodes in the treatment when compared to control.

We next hypothesized that the immunomodulatory effects of our hydrogel treatment would likely modulate the adaptive immune system. We performed flow cytometry on isolated tissue from the window chamber, adding CD3$^+$, CD4$^+$, CD25$^+$, and CD8$^+$ markers for adaptive immunity. We aimed to identify T-cell involvement by using a base CD3$^+$ SPADE dendrogram. We first identified CD4$^+$ CD25$^+$ T-regulatory cells using SPADE (Fig. 7C). We then created tornado plots to observe the difference in cell frequency in the treatment from control samples to identify shifts in cellular heterogeneity. Unfortunately, we did not observe any CD4$^+$ CD25$^+$ nodes that had increased cell frequency per node in either control or treatment. (Fig. 7D). Notably, we observed an increased number of nodes in AT-RvD1 treatment alone compared to treatment, mirroring a similar result which was observed in IL-10+ DCs. Finally, we also identified the presence of a CD8$^+$ IL-10+ subpopulation of cells, which was particularly abundant in the dual hydrogel group. This CD8$^+$ IL-10+ co-expressing cell was most abundant in nodes in treatment group in the dual IL-10+AT-RvD1 over control (Fig. 7E and F).

3. Discussion

The use of biomaterial implants to deliver cells or bioactive molecules capable of directing the host immune response after injury can modulate processes critical to the restoration of tissue homeostasis, such as cellular cytokine release, vascular remodeling, or deposition of extracellular matrix [2]. It is becoming increasingly apparent that these processes are regulated not only by cells of the innate immune system, such as monocytes and macrophages, but that cells of the adaptive immune system play active and important roles [43]. Here, we aimed to develop a material that can enrich the wound microenvironment with anti-inflammatory cells of both the innate and adaptive immune system to enhance the regenerative response.

Integrin signaling appears to play different roles in leukocyte migration, depending on the environment in which the cell is migrating. For example, monocytes utilize the integrin LFA-1 to crawl along the endothelium and extravasate into the tissue [9,44]. Conversely, leukocyte migration through interstitial space is not integrin-dependent and instead involves amoeboid-like flowing and squeezing motions [44]. The critical parameter appears to be whether the cell comes in contact with a 2D barrier, such as the endothelium. Biomaterials provide a unique context to migrating cells, where the surface serves as a 2D barrier, but materials that are porous or have topographical features may be interpreted by cells as an analogous environment to interstitial space. Here, we demonstrate that CX3CR1+ myeloid cells move at greater speeds near hydrogels presenting integrin ligands. This effect appears to be primarily localized to the material surface, as we observed increased mean velocity around R<u>G</u>D hydrogels compared to R<u>D</u>G hydrogels only if the cells were within 30 μm

of the hydrogel surface. There was no difference in migration speed between RGD- and RDG-functionalized materials at distances greater than 30 μm.

To achieve a higher level of control over both innate and adaptive immune cell recruitment, we developed a hydrogel-based system capable of the dual delivery of two factors critical for the recruitment and activation of pro-regenerative cells of both the myeloid and lymphoid lineages. PEG-4MAL hydrogels were used to achieve *in vivo* release of both AT-RvD1 and IL-10. This dual-release profile will allow for fast release of AT-RvD1 after *in situ* hydrogel gelation to target the myeloid first responders followed by a more gradual release over time of thiolated IL-10 to influence the activity of cells involved in the later stages of the inflammatory response, mimicking the natural progression of the immune response. This PEG-4MAL system allows for the incorporation of adhesive peptides into the hydrogel backbone, as well as control over gelling and degradation kinetics through the modification of component pH and chosen peptide crosslinker [45]. Without the addition of thiol groups, approximately 90% of the loaded unmodified IL-10 was released *in vitro* after 24 h. After thiolation, the release of IL-10 was much slower, with nearly 70% of the loaded IL-10 remaining in the gel at day 5. Of note, this was observed in the absence of proteases that would degrade the gel. The thiolated IL-10 was also able to modulate the expression of TNF-α in RAW264.7 macrophages following LPS treatment, indicating that thiolation does not affect the ability of IL-10 to modulate pro-inflammatory responses after inflammatory stimulus. The AT-RvD1, which was not tethered to the PEG-MAL backbone, was delivered from the hydrogel primarily in a burst release over the first 24 h, consistent with our previous release kinetics from AT-RvD1-loaded PLGA thin films [16].

Post-injury vascular remodeling is a crucial step in the tissue repair process that is necessary to ensure the delivery of nutrients and recruited cells to the regenerating tissue. The vascular network is expanded via formation of new vessels and by remodeling existing vasculature to support increased blood flow. This vascular network expansion is carried out in coordination with recruited leukocytes of many varieties, including monocytes, macrophages and T lymphocytes [46–48]. Leukocytes are able to drive this process through the secretion of growth factors and matrix-remodeling enzymes [46,49–54]. We have previously shown that local delivery of the bioactive sphingolipid mimicking pro-drug FTY720, chemokine stromal-derived factor 1α (SDF-1α), and AT-RvD1 are able to promote vascular remodeling processes [55,56]. In this study, we show that immunomodulatory biomaterials loaded with IL-10, AT-RvD1, or combination are able to affect vascular remodeling over time. IL-10 single therapy is able to enhance arteriolar enlargement but is not able to promote expansion of the vascular network. On the other hand, AT-RvD1 and dual IL-10+AT-RvD1 treatments significantly increased both arteriolar caliber and vascular network length density, indicating a remodeling of existing vasculature as well as expansion of new vessels. While we cannot definitively prescribe a mechanism underlying these findings, increased vascular network expansion may be associated with non-classical monocyte and M2 macrophage accumulation observed after AT-RvD1 therapy that was not seen following IL-10-only therapy.

The accumulation of immune cells in injured tissue is important in the process of restoring tissue homeostasis after injury, but perhaps more important is the cellular

phenotype and effector functions [57]. For example, monocytes and macrophages exist on a spectrum of activation ranging from pro-to anti-inflammatory, with the M1 CD86+CD206- phenotype considered to be more pro-inflammatory, and the M2 CD86− CD206+ phenotype considered to be more anti-inflammatory [48]. Several studies have further characterized macrophage MerTK + CD64+ populations into Ly6C high (Ly6Chi) or low (Ly6Clo). It has been suggested that after wounding, MerTK expression is higher on Ly6Clo than Ly6Chi cells. MerTK + Ly6Clo populations resemble anti-inflammatory macrophage populations, producing cytokines consistent with wound repair, and Ly6Chi populations have more pro-inflammatory capabilities [14,19,58]. Persistent accumulation and activation of M1 macrophages has been associated with disease states such as type 2 diabetes and atherosclerosis [59], but complete blockage of M1 pathways has been associated with impaired tissue repair and wound healing [60]. When designing immunomodulatory materials with the overall goal of ameliorating inflammation and promoting tissue repair, it is important to consider the necessary balance between allowing pro-inflammatory signaling to occur and amplifying anti-inflammatory signals, as both are needed in the regenerative process [61]. Indeed, allowing an unabated "M2-like" anti-inflammatory response can result in excessive tissue remodeling and fibrosis [17]. We subcutaneously injected immunomodulatory hydrogels containing IL-10, AT-RVD1, or a combination of these factors into excisional skin wounds and chronicled the immune response to these hydrogels over time. We observed significant decreases in the recruitment of circulating pro-inflammatory immune cells following delivery of immunomodulatory hydrogels – namely, hydrogels containing AT-RvD1 dampened local neutrophil infiltration, while IL-10 and AT-RvD1 treatment modulated Ly6Chi monocyte infiltration (Supplementary figure 2). However, these treatments were not able to completely block the recruitment of these pro-inflammatory cells. Additionally, we saw a transient increase in M1 macrophages after one day followed by a significant decrease in this population by day 7 in animals treated with AT-RvD1 or the combination hydrogels. Taken together, these findings indicate that while these immunomodulatory hydrogels are indeed capable of modulating the immune system, they still allow for the necessary actions of "pro-inflammatory" cell subsets. On the other hand, the recruitment of Ly6CLow monocytes and M2 macrophages was significantly increased at days 3 and 7 following AT-RvD1 treatment. Interestingly, IL-10 only treatment was not able to modulate the recruitment of these immune cell subsets, but dual delivery of IL-10 and AT-RvD1 significantly increased these populations compared to AT-RvD1-only hydrogels, indicating the existence of a synergistic feed-forward mechanism between AT-RvD1 and IL-10 that is able to amplify the recruitment of differentiation of these anti-inflammatory cells. Our finding of increased CD206+ M2 macrophages via flow cytometric analysis was further supported using analysis of whole mount immunohistochemistry, where we observed significantly more CD68+CD206+ cells in the peri-implant dorsal tissue by day 7. In order to further elucidate the cellular heterogeneity of the macrophage populations at day 7, we utilized SPADE, a dimensionality reduction technique that hierarchically clusters phenotypically similar cells into "nodes", which are then organized into a minimum spanning tree, or "SPADE tree" [42,62–64]. Each SPADE node carries a unique profile of surface marker expression, from which we were able to identify the change in immune cell frequency in response to immunomodulatory hydrogel treatment. SPADE analysis indicated three nodes out of a MerTK + CD64+ SPADE dendrogram that were dominated by M1

macrophages. We then created "tornado plots" to elucidate whether the cellular frequency was more abundant in control or treatment groups by subtracting percent cellular frequency in treatment groups from control groups. In the M1 macrophage identified nodes, we observed a shift in cellular frequency towards control over treatment groups. Interesting, we observed 26 nodes dominated by CD206+ cells, which we further subdivided into Ly6C high or low and MHC-II+/−. In the tornado plots, we notice mixed Ly6C expression in IL-10 alone and AT-RvD1 alone treatment and control groups. However, in IL-10+AT-RvD1, we observed M2 nodes dominated by LyClo MHC-II + nodes in treatment groups, consistent with wound repair phenotypes, whereas the control group was mixed between LyChi and Ly6Clo expression. Notably, M2 populations exist in at least three polarization states, deemed M2A, M2b, and M2c [65]. M2a and M2c have similar effector functions, but M2c is polarized by IL-10, whereas M2a is polarized in the presence of IL-4 [66]. Dual delivery of AT-RvD1 and IL-10 could increase the M2c pool, thereby expanding the overall CD206+ population. SPADE analysis confirms that the M2 population in response to injury is highly heterogeneous, and future studies should include other surface, intracellular, and activation markers to further elucidate M2 phenotypes.

It was then our goal to expand our inquiry into cell subsets involved in wound healing that we have not explored previously, dendritic cells and lymphocytes. "Tolerogenic DCs" or DC-10s, are polarized by IL-10, have the ability to signal to Treg populations and promote their activity. Additionally, these tolerogenic DCs have been shown to improve cardiac function and survival after myocardial infarction through the induction of Tregs and promotion of neovascularization and amelioration of pathologic left ventricle wall remodeling [67]. Due to these actions, IL-10+ DCs may serve as a cellular bridge between the pro-regenerative arms of the innate and adaptive immune systems. We also observed significant decreases in overall expression of TNF-α within the DC population among all groups compared to control, indicating the ability of all treatments to diminish the pro-inflammatory activity of immune cells. By day 7, flow cytometric and whole mount immunohistochemistry analysis showed that IL-10+AT-RvD1 combination treatment significantly expanded the population of IL-10+ DCs. When we measured IL-10 staining via IHC, we saw additional IL-10 that was not colocalized with CD11c. This IL-10 staining could be extracellular IL-10 that has been released from cells and is in the interstitial tissue. The IL-10 could also be intracellular IL-10 present within Tregs. Future analyses could modify our IHC staining panels to include a T cell marker to visualize the contributions of these cells. In addition, SPADE analysis showed an increase in IL-10 + DCs in treatment over control groups in all treatment groups. In particular, we observed a complete dominance of IL-10+ DC nodes by the dual hydrogel treatment group when compared to control. Future studies should include additional cell surface and cellular expression markers to further elucidate this result.

Because of the increase in IL-10+ DCs by flow cytometry and SPADE, we aimed to identify the effects of immunomodulatory hydrogel treatment on adaptive immune cell populations using SPADE. SPADE analysis of CD4^{+} CD25^{+} Tregs did not show any changes in cellular frequency in response to IL-10 alone, AT-RvD1 alone, or dual hydrogel treatment. Interestingly, however, SPADE revealed the surprising finding of CD8^{+} IL-10+ T-cell subpopulations. This subset of cells was particularly abundant in nodes whose

cellular frequency was increased in treatment IL-10+AT-RvD1 compared to control. This subpopulation was not observed in either treatment alone. CD8$^+$ Tregs have been shown to be induced via IL-4 and IL-10 and subsequently are able to produce IL-10 [68]. It has been shown that CD8 Tregs are induced during mucosal tolerance, and allospecific CD8 Tregs have be used as immunotherapy to block T-helper 2 cell (Th2) activation (65). Moreover, manipulation of CD8 Tregs have been implicated for delayed donor T-cell transfusion in GVHD [68,69]. In addition, CD8$^+$ Tregs have been suggested to play a role in regulating acute or chronic inflammation [70]. These data suggest a unique role for the adaptive immune system in response to biomaterials at the injury site.

Our data shows a synergistic interplay between AT-RvD1 and IL-10 that allows for increased control of the recruitment of cells from the innate and adaptive immune system compared to either treatment on its own. Moreover, this data indicates an interesting role for CD8$^+$ Tregs in the process of wound healing. In large wounds, or in diseases states, immune dysregulation prevents normal tissue regeneration, potentially leading to a chronic inflammatory state. This study employs a novel therapeutic hydrogel for wound resolution, as well as a novel method in which a dimensionality-reduction technique, SPADE, is used to make cellular hierarchy inferences among subpopulations of macrophages, dendritic cells, and T-cells. Our studies can be used to explore cellular hierarchies and thus, rationally design future biomaterials for regenerative immunotherapies. This dual-delivery system has the potential to improve therapeutic wound healing outcomes following trauma or tissue transplantation via synergy of cellular recruitment and polarization processes to promote anti-inflammatory cell recruitment and activity.

4. Materials and methods

4.1. RGD and RDG poly(ethylene) glycol hydrogel synthesis

Four-arm poly (ethylene glycol) (PEG, 20 kDA molecular weight) end-functionalized with maleimide (>95% purity, Laysan Bio) at 4.5% weight/volume was used for all hydrogel formulations. PEG macromers were functionalized with RGD peptide (GRGDSPC), or RDG scrambled peptide control (GRDGSPC), and crosslinked with the cysteine-flanked peptide VPM (GCRDVPMSMRGGDRCG) (AAPPTec) in 0.5 M MES buffer, pH 5.5. The final concentration of RGD was 1.0 mM. The cross-linker concentration was based on the concentration of non-reacted maleimide groups remaining on PEG macromers. To generate pre-formed hydrogels for intravital imaging, the hydrogel was cast in a 4 mm diameter circular silicon mold. After crosslinking, hydrogels were incubated at 37 °C for 15 min and then swelled in PBS for at least 30 min. For studies where hydrogels were fluorescently tagged, RGD or RDG was dissolved in sodium bicarbonate and tagged with Alexa Fluor 405 NHS Ester (Life Technologies) according to the manufacturer's recommendation. Tagged RGD or RDG was combined with unlabeled peptide in a 1:3 ratio for conjugation to PEG-MAL.

4.2. Thiolation of IL-10

Carrier-free recombinant human IL-10 was purchased from BioLegend. IL-10 was thiolated using 30 M excess of Traut's reagent (Sigma) for 1 h in PBS containing 0.1 µL EDTA

per uL buffer to chelate free metals. The thiolation reaction was shaken at RT for 1 h. Thiolated IL-10 was separated from unreacted Traut's reagent using a Zeba desalting column according to manufacturer's instructions. Thiolation was detected using a Measure-IT™ Thiol Assay Kit (Invitrogen) according to kit instructions. Number of thiol groups per IL-10 was calculated using the concentration of detected thiols and the known concentration of IL-10 in each measured sample.

4.3. Hydrogel loading of IL-10 and AT-RvD1

For hydrogels used in animal studies, all components were filtered through a spin column after pH measurements and kept under sterile conditions until injection into the animals. To generate pre-formed hydrogels for release studies, the hydrogel was formed on a sterilized Petri dish. After crosslinking, hydrogels were incubated at 37 °C for 15 min and then swelled in PBS for at least 30 min. Release of thiolated and unthiolated IL-10 was measured over time in 1% BSA solution using IL-10 tagged with Alexa Fluor 405 NHS Ester (Life Technologies) according to the manufacturer's recommendation and quantified using a standard curve of known fluorescent IL-10 concentrations. Release of AT-RvD1 was measured with a Shimadzu UFLC High Performance Liquid Chromatograph (Columbia, MD, USA) equipped with a Shimadzu Premier C18, 5 μm (250 × 4.6 mm) column. AT-RvD1 elution was measured at 8.6 min using a wavelength of 301 nm. Known quantities of AT-RvD1 were used to generate a standard curve relating AT-RvD1 mass to total peak area. Using serial dilutions, we determined that the limit of detection was below 0.5 pg/μL. The total amount of AT-RvD1 in each release sample was calculated using the standard curve.

4.4. Macrophage TNF-α expression assay

Expression of TNF-α by RAW264.7 murine macrophages after treatment with Lipopolysaccharide (LPS) was used as an *in vitro* functional metric for measuring bioactivity of IL-10 and AT-RvD1. One million RAW264.7 cells were cultured in 6 well plates with Dulbecco's modified Eagle medium (Gibco) containing 1 mM sodium pyruvate (Gibco) and 2 mM L-glutamine (Gibco) supplemented with 10% Fetal Bovine Serum (FBS, Gibco). Cells were pretreated with IL-10, thiolated IL-10, PEGylated thiolated IL-10, AT-RvD1, AT-RvD1 and thiolated IL-10 combination, or control PBS for 1 h. Pretreatment dosages were equal to dosages loaded into hydrogels. Pretreatment was removed and cells were washed once with PBS. Cells were then stimulated with 50 ng/ mL LPS for 2 h in 2 mL media supplemented with 100 μL Brefeldin-A (manufacturer) per mL cell culture media. Cells were removed from wells and fixed with 4% paraformaldehyde for 30 min at RT. Cells were permeabilized through two washes of PBS containing 1% FBS and 0.1% Saponin. Cells were stained for TNF- α (eBioscience) and TNF- α staining was detected using a FACS-AriaIIIu flow cytometer (BD Biosciences).

4.5. Dorsal skinfold window chamber surgery

Animal experiments were performed using sterile techniques in accordance with an approved protocol form the Georgia Institute of Technology Institutional Animal Care and Use Committee. Male C57BL/ 6 mice (Jackson) aged 6–12 weeks were anesthetized by inhaled isofluorane and surgically fitted with sterile dorsal skinfold window chambers (APJ Trading Co.) as previously described [16]. Briefly, the dorsal skin was shaved, depilated,

and sterilized via three washes with 70% ethanol and chlorhexidine. The dorsal skin was drawn away from the back of the mouse and one side of the titanium frame was attached to the underside of the skin. Sterile surgical micro scissors were then used to expose the microvasculature through the removal of the epidermis and dermis in a 12 mm diameter circle. 25 μl sterile hydrogels were then mixed, drawn into a syringe, and injected underneath the exposed vascular bed. For internally controlled experiments, the unloaded control hydrogel was injected on the caudal side of the window chamber, and the loaded hydrogel was injected rostrally. Exposed tissue was then sealed with a sterile glass coverslip. Mice were administered sustained-released buprenorphine i. p. (0.1–0.2 mg/kg) and allowed to recover in heated cages. All mice received standard laboratory diet and water ad libitum throughout the course of the experiment.

4.6. Vascular metrics

Mice were anesthetized with isofluorane, the glass window was removed, and dorsal tissue was superfused with adenosine in Ringer's solution (1 mM) to prevent desiccation and to maximally dilate exposed vessels. The mouse was mounted on a microscope stage and imaged non-invasively at 5× magnification on a Zeiss Imager. D2 microscope with AxioCam MRC 5 color digital camera (Zeiss). Images were acquired on day 0 immediately following film implantation and again on days 3 and 7. Microvascular length density measurements were made within a 4000×4000 pixel square region of interest (ROI) around the film. Vessels within these ROIs were traced and total vessel length per unit area was quantified via ImageJ. Arteriolar diameter measurements were made within the ROIs by identifying arteriolar-venular pairs at day 0. Internal diameter changes were measured via ImageJ and days 3 and 7 diameters were normalized to day 0.

4.7. Tissue harvest and flow cytometry

To collect samples for flow cytometry analysis, mice were euthanized via CO_2 asphyxiation. The dorsal tissue was excised and digested with collagenase type 1-A (1 mg/mL, Sigma) at 37 °C for 30 min and further separated with a cell strainer to create a single cell suspension. Single cell suspensions of dorsal tissue were stained for flow cytometry analysis using standard methods and analyzed on a FACS-AriaIIIu flow cytometer (BD Biosciences). Dead cells were excluded through staining using Zombie Red fixable viability stain (BioLegend). The antibodies used for identifying cell populations of interest were: PE conjugated MerTK (Biolegend), PE-Cy7 conjugated MHC-II (BioLegend), BV605 conjugated CD206 (BioLegend), BV510 conjugated Ly6C (BioLegend), APC-Cy7 conjugated Ly6G (BioLegend), BV711 conjugated CD64 (BioLegend), BV785 conjugated CD19 (BioLegend), APC conjugated Cd11 b (BioLegend), BV421 conjugated CD11c (Biolegend, FITC conjugated CD86 (BioLegend), PerCP-Cy5.5 conjugated CD3 (Biolegend), BV785 conjugated CD8 (BioLegend), BV605 conjugated CD4 (BioLegend), and BV711 conjugated CD25 (BioLegend). Staining using BV dyes was performed in the presence of Brilliant Stain Buffer (BD Biosciences). Cells were stained for intracellular cytokines using PE conjugated IL-10 (BioLegend) and PE-Cy7 conjugated TNF- α (eBiosciences). Positivity was determined by gating on fluorescence minus one controls. Absolute quantification of cell numbers was performed by adding 25 μL of AccuCheck counting beads to flow cytometry samples (Thermo Fisher Scientific).

4.8. Intravital confocal microscopy

CX3CR1-GFP mice were anesthetized with vaporized isoflurane at 5% concentration for induction and maintained under anesthesia at 1–3%. The glass cover slip was removed, and sterile saline was administered to the exposed dorsal tissue to prevent desiccation. The anesthetized mouse was secured to the microscope stage in a custom adapter placed on top of a heating block to maintain body temperature. Intravital confocal microscopy was performed using a 20× water immersion objective (NA = 1.0) fixed to an inverter on a Zeiss LSM710 NLO microscope. Time-lapse z-stack images were acquired at each hydrogel edge. A step size of 5 μm was used in the z-direction. Videos of 25–30 min were acquired at each location, with a time step of 30 s and a total of 2–3 videos acquired for each hydrogel, and one video acquired in distal tissue without a hydrogel.

4.9. Intravital imaging analysis

For 3D analysis in Imaris (Bitplane), time-lapse images were acquired adjacent to the implant to visualize immune cell distribution in the close surrounding tissue. Cells expressing CX3CR1-GFP were identified in Imaris using the surface tool. CX3CR1+ surfaces were identified by smoothing with a 2.77 μm grain size and a threshold value of 7.71 on absolute intensity. Touching objects were split using a seed points diameter of 10.4 μm with a quality threshold above 3.53. CX3CR1^{hi} versus CX3CR1^{lo} cells were discriminated by assigning half of all cells to each group based on maximum fluorescence intensity in the CX3CR1- GFP channel. The hydrogel surface was identified using the surface tool with a 10 μm grain size and a manually selected threshold value on absolute intensity. To calculate the distance between cells and the hydrogel surface, a distance transformation was applied to the hydrogel surface and the minimum distance of each cell was recorded. To track cell activity over time, cells were identified in Imaris using the spots tool. Estimated diameter was set to 8.00 μm with background subtraction enabled and an automatic threshold on quality. Tracks were selected for analysis if they lasted at least 300 s. Tracks were set to a maximum distance of 10.0 μm and a max gap size of 3 μm. Because statistical comparisons were made on a single-cell basis, an equal number of cells was used for analysis of each video. The minimum number of detected tracks was 73. Therefore, for videos with more than 73 tracks, we randomly selected 73 tracks for analysis.

4.10. Tissue whole mount immunohistochemistry and confocal imaging

Following euthanasia, mouse vasculature was perfused with warm saline and then with 4% paraformaldehyde until tissues were fixed. The dorsal tissue was excised and permeabilized overnight at 4 °C with 0.2% saponin. The tissues were blocked overnight in 10% mouse serum at 4 °C. Tissues were incubated at 4 °C overnight in staining solution containing 0.1% saponin, 5% mouse serum, 0.5% fatty-acid free bovine serum albumin, and the following fluorescently conjugated mouse antibodies: Alexa Fluor 594 anti-CD31 antibody (1:100 dilution, BioLegend) for blood vessel visualization, Brilliant Violet 421 anti-CD68 (1:200 dilution, BioLegend) for visualization of macrophages, and Alexa Fluor 647 anti-CD206 (1:200 dilution, Biolegend) for visualization of M2 macrophages. The following unconjugated antibodies were also used: Biotin anti-CD11c (1:200 dilution, BioLegend) for visualization of dendritic cells, and Rabbit polyclonal anti-IL-10 (1:200 dilution). Tissues

were washed four times for 30 min with 0.2% saponin and stained with Streptavidin-conjugated Alexafluor 430 (1:200 dilution, Invitrogen) and Goat anti-rabbit Alexa Fluor 488 (1:200 dilution, Abcam) secondary antibodies for 4 h at room temperature. Tissues were washed twice for 30 min with 0.2% saponin and again overnight at 4 °C. Specimens were then washed once in PBS for 30 min and mounted in 50/ 50 glycerol/phosphate buffered saline. Mounted samples were imaged on a Zeiss LSM 710 NLO confocal.

4.11. SPADE analysis of flow cytometry data

Dimensionality reduction analysis was performed using MATLAB-based Spanning-tree Progression Analysis of Density-normalized Events (SPADE). SPADE is a computational technique that performs density-dependent down-sampling, agglomerative clustering, linking clusters using minimum spanning-tree algorithm, and finally, up- samples based on user input. The SPADE trees generated here were generated by exporting compensated pre-gated single cells, CD11b + myeloid cells, MerTK + CD64$^+$ cells; single cells, CD3$^-$, CD11c + cells; or pre-gated single cells, CD3$^+$ cells. The markers used to build the SPADE tree were SSC, FSC, CD11b, Ly6G, CD11c, CD64, CD86, CD206, CD8, CD4, CD25, Ly6C, IL-10, TNF-a. The following SPADE parameters were used: Apply compensation matrix in FCS header, Arcsinh transformation with cofactor 150, neighborhood size 5, local density approximation factor 1.5, max allowable cells in pooled downsampled data 50000, target density 20000 cells remaining, and number of desired clusters 100.

5. Statistical analysis

All statistical analyses were performed using Graphpad Prism version 6.0 (La Jolla, CA). Results are presented as mean ± standard error of the mean (SEM). For grouped analyses, one-way ANOVA with Tukey's post- test was used for multiple comparisons. For internally controlled experiments, two-way ANOVA was used. Tukey's post-hoc test was utilized when comparing paired samples, and Bonferroni's post hoc test was employed when comparing between treatment groups. Unless otherwise noted, $p < 0.05$ was considered statistically significant.

Supplementary Material

Refer to Web version on PubMed Central for supplementary material.

Acknowledgments

References

[1]. Rankin LC, Artis D, Beyond host defense: emerging functions of the immune system in regulating complex tissue physiology, Cell 173 (3) (2018) 554–567. [PubMed: 29677509]

[2]. Larouche J, Sheoran S, Maruyama K, Martino MM, Immune regulation of skin wound healing: mechanisms and novel therapeutic targets, Adv. Wound Care 7 (7) (2018) 209–231.

[3]. Atala A, Irvine DJ, Moses M, Shaunak S, Wound healing versus regeneration: role of the tissue environment in regenerative medicine, MRS Bull. 35 (8) (2010).

[4]. Nathan C, Neutrophils and immunity: challenges and opportunities, Nat. Rev. Immunol 6 (3) (2006) 173–182. [PubMed: 16498448]

[5]. Ebaid H, Neutrophil depletion in the early inflammatory phase delayed cutaneous wound healing in older rats: improvements due to the use of un-denatured camel whey protein, Diagn. Pathol 9 (2014) 46. [PubMed: 24593823]

[6]. Godwin JW, Pinto AR, Rosenthal NA, Macrophages are required for adult salamander limb regeneration, Proc. Natl. Acad. Sci. U. S. A 110 (23) (2013) 9415–9420. [PubMed: 23690624]

[7]. Li L, Yan B, Shi YQ, Zhang WQ, Wen ZL, Live imaging reveals differing roles of macrophages and neutrophils during zebrafish tail fin regeneration, J. Biol. Chem 287 (30) (2012) 25353–25360. [PubMed: 22573321]

[8]. Geissmann F, Jung S, Littman DR, Blood monocytes consist of two principal subsets with distinct migratory properties, Immunity 19 (1) (2003) 71–82. [PubMed: 12871640]

[9]. Auffray C, Fogg D, Garfa M, Elain G, Join-Lambert O, Kayal S, Sarnacki S, Cumano A, Lauvau G, Geissmann F, Monitoring of blood vessels and tissues by a population of monocytes with patrolling behavior, Science 317 (5838) (2007) 666–670. [PubMed: 17673663]

[10]. Carlin LM, Auffray C, Geissmann F, Measuring intravascular migration of mouse Ly6C(low) monocytes in vivo using intravital microscopy, Curr Protoc Immunol Chapter 14 (2013). Unit 14 33 1–16.

[11]. Carlin LM, Stamatiades EG, Auffray C, Hanna RN, Glover L, Vizcay- Barrena G, Hedrick CC, Cook HT, Diebold S, Geissmann F, Nr4a1-dependent Ly6C (low) monocytes monitor endothelial cells and orchestrate their disposal, Cell 153 (2) (2013) 362–375. [PubMed: 23582326]

[12]. Collison JL, Carlin LM, Eichmann M, Geissmann F, Peakman M, Heterogeneity in the locomotory behavior of human monocyte subsets over human vascular endothelium in vitro, J. Immunol 195 (3) (2015) 1162–1170. [PubMed: 26085686]

[13]. Ogle ME, Krieger JR, Tellier LE, McFaline-Figueroa J, Temenoff JS, Botchwey EA, Dual affinity heparin-based hydrogels achieve pro-regenerative immunomodulation and microvascular remodeling, ACS Biomater. Sci. Eng 4 (4) (2018) 1241–1250. [PubMed: 29682605]

[14]. Olingy CE, San Emeterio CL, Ogle ME, Krieger JR, Bruce AC, Pfau DD, Jordan BT, Peirce SM, Botchwey EA, Non-classical monocytes are biased progenitors of wound healing macrophages during soft tissue injury, Sci. Rep 7 (1) (2017) 447. [PubMed: 28348370]

[15]. San Emeterio CL, Olingy CE, Chu Y, Botchwey EA, Selective recruitment of non-classical monocytes promotes skeletal muscle repair, Biomaterials 117 (2017) 32–43. [PubMed: 27930948]

[16]. Sok MCP, Tria MC, Olingy CE, San Emeterio CL, Botchwey EA, Aspirin- Triggered Resolvin D1-modified materials promote the accumulation of pro- regenerative immune cell subsets and enhance vascular remodeling, Acta Biomater. 53 (2017) 109–122. [PubMed: 28213094]

[17]. Wermuth PJ, Jimenez SA, The significance of macrophage polarization subtypes for animal models of tissue fibrosis and human fibrotic diseases, Clin. Transl. Med 4 (2015) 2. [PubMed: 25852818]

[18]. Shechter R, Miller O, Yovel G, Rosenzweig N, London A, Ruckh J, Kim KW, Klein E, Kalchenko V, Bendel P, Lira SA, Jung S, Schwartz M, Recruitment of beneficial M2 macrophages to injured spinal cord is orchestrated by remote brain choroid plexus, Immunity 38 (3) (2013) 555–569. [PubMed: 23477737]

[19]. Crane MJ, Daley JM, van Houtte O, Brancato SK, Henry WL Jr., J.E. Albina, The monocyte to macrophage transition in the murine sterile wound, PloS One 9 (1) (2014), e86660.

[20]. Ogle ME, Segar CE, Sridhar S, Botchwey EA, Monocytes and macrophages in tissue repair: implications for immunoregenerative biomaterial design, Exp. Biol. Med 241 (10) (2016) 1084–1097.

[21]. Mokarram N, Merchant A, Mukhatyar V, Patel G, Bellamkonda RV, Effect of modulating macrophage phenotype on peripheral nerve repair, Biomaterials 33 (34) (2012) 8793–8801. [PubMed: 22979988]

[22]. Awojoodu AO, Ogle ME, Sefcik LS, Bowers DT, Martin K, Brayman KL, Lynch KR, Peirce-Cottler SM, Botchwey E, Sphingosine 1-phosphate receptor 3 regulates recruitment of anti-

inflammatory monocytes to microvessels during implant arteriogenesis, Proc. Natl. Acad. Sci. U. S. A 110 (34) (2013) 13785–13790.

[23]. Krieger JR, Ogle ME, McFaline-Figueroa J, Segar CE, Temenoff JS, Botchwey EA, Spatially localized recruitment of anti-inflammatory monocytes by SDF-1alpha-releasing hydrogels enhances microvascular network remodeling, Biomaterials 77 (2016) 280–290. [PubMed: 26613543]

[24]. Sadtler K, Estrellas K, Allen BW, Wolf MT, Fan H, Tam AJ, Patel CH, Luber BS, Wang H, Wagner KR, Powell JD, Housseau F, Pardoll DM, Elisseeff JH, Developing a pro-regenerative biomaterial scaffold microenvironment requires T helper 2 cells, Science 352 (6283) (2016) 366–370. [PubMed: 27081073]

[25]. Gaudino SJ, Kumar P, Cross-talk between antigen presenting cells and T cells impacts intestinal homeostasis, bacterial infections, and tumorigenesis, Front. Immunol 10 (2019) 360. [PubMed: 30894857]

[26]. Worbs T, Hammerschmidt SI, Forster R, Dendritic cell migration in health and disease, Nat. Rev. Immunol 17 (1) (2017) 30–48. [PubMed: 27890914]

[27]. Maldonado RA, von Andrian UH, How tolerogenic dendritic cells induce regulatory T cells, Adv. Immunol 108 (2010) 111–165. [PubMed: 21056730]

[28]. Bracho-Sanchez E, Lewis JS, Keselowsky BG, Biomaterials-based immunomodulation of dendritic cells, in: Santambrogio L(Ed.), Biomaterials in Regenerative Medicine and the Immune System, Springer International Publishing, Cham, 2015, pp. 139–156.

[29]. Hwu P, Du MX, Lapointe R, Do M, Taylor MW, Young HA, Indoleamine 2,3-dioxygenase production by human dendritic cells results in the inhibition of T cell proliferation, J. Immunol 164 (7) (2000) 3596–3599. [PubMed: 10725715]

[30]. Zhang X, Chen G, Liu Y, Sun L, Sun L, Zhao Y, Black phosphorus-loaded separable microneedles as responsive oxygen delivery carriers for wound healing, ACS Nano 14 (5) (2020) 5901–5908. [PubMed: 32315159]

[31]. Lee CH, Resolvins as new fascinating drug candidates for inflammatory diseases, Arch Pharm. Res. (Seoul) (2012) 3–7.

[32]. Chen J, Shetty S, Zhang P, Gao R, Hu Y, Wang S, Li Z, Fu J, Aspirin-triggered resolvin D1 down-regulates inflammatory responses and protects against endotoxin-induced acute kidney injury, Toxicol. Appl. Pharmacol 277 (2) (2014) 118–123. [PubMed: 24709673]

[33]. Hong S, Lu Y, Yang R, Gotlinger KH, Petasis NA, Serhan CN, Resolvin D1, protectin D1, and related docosahexaenoic acid-derived products: analysis via electrospray/low energy tandem mass spectrometry based on spectra and fragmentation mechanisms, J. Am. Soc. Mass Spectrom (2007) 128–144. [PubMed: 17055291]

[34]. Levy BD, Resolvins and protectins Natural pharmacophores for resolution biology, Prostaglandins Leukotrienes & Essential Fatty Acids, Elsevier (2010) 327–332.

[35]. Ouyang W, Rutz S, Crellin NK, Valdez PA, Hymowitz SG, Regulation and functions of the IL-10 family of cytokines in inflammation and disease, Annu. Rev. Immunol 29 (2011) 71–109. [PubMed: 21166540]

[36]. Boks MA, Kager-Groenland JR, Haasjes MS, Zwaginga JJ, van Ham SM, ten Brinke A, IL-10-generated tolerogenic dendritic cells are optimal for functional regulatory T cell induction–a comparative study of human clinical-applicable DC, Clin. Immunol 142 (3) (2012) 332–342. [PubMed: 22225835]

[37]. Orecchioni M, Ghosheh Y, Pramod AB, Ley K, Macrophage polarization: different gene signatures in M1(LPS+) vs. Classically and M2(LPS–) vs. Alternatively activated macrophages, Front. Immunol 10 (2019) 1084. [PubMed: 31178859]

[38]. Hume PS, He J, Haskins K, Anseth KS, Strategies to reduce dendritic cell activation through functional biomaterial design, Biomaterials 33 (14) (2012) 3615–3625. [PubMed: 22361099]

[39]. Mauri E, Sacchetti A, Rossi F, The synthesis of RGD-functionalized hydrogels as a tool for therapeutic applications, JoVE 116 (2016).

[40]. Dagvadorj J, Naiki Y, Tumurkhuu G, Hassan F, Islam S, Koide N, Mori I, Yoshida T, Yokochi T, Interleukin-10 inhibits tumor necrosis factor-alpha production in lipopolysaccharide-stimulated

RAW 264.7 cells through reduced MyD88 expression, Innate Immun. 14 (2) (2008) 109–115. [PubMed: 18713727]

[41]. Gordon S, Pluddemann A, Martinez Estrada F, Macrophage heterogeneity in tissues: phenotypic diversity and functions, Immunol. Rev 262 (1) (2014) 36–55. [PubMed: 25319326]

[42]. Qiu P, Simonds EF, Bendall SC, Gibbs KD Jr., R.V. Bruggner, M.D. Linderman, K. Sachs, G.P. Nolan, S.K. Plevritis, Extracting a cellular hierarchy from high- dimensional cytometry data with SPADE, Nat. Biotechnol 29 (10) (2011) 886–891. [PubMed: 21964415]

[43]. Janeway Ca TP Jr., Walport M, et al. , Immunobiology: the Immune System in Health and Disease, Garland Science, New York, 2001.

[44]. Lammermann T, Bader BL, Monkley SJ, Worbs T, Wedlich-Soldner R, Hirsch K, Keller M, Forster R, Critchley DR, Fassler R, Sixt M, Rapid leukocyte migration by integrin-independent flowing and squeezing, Nature 453 (7191) (2008) 51–55. [PubMed: 18451854]

[45]. Phelps EA, Enemchukwu NO, Fiore VF, Sy JC, Murthy N, Sulchek TA, Barker TH, Garcia AJ, Maleimide cross-linked bioactive PEG hydrogel exhibits improved reaction kinetics and cross-linking for cell encapsulation and in situ delivery, Adv Mater 24 (1) (2012) 64–70, 2. [PubMed: 22174081]

[46]. Takeda Y, Costa S, Delamarre E, Roncal C, Leite de Oliveira R, Squadrito ML, Finisguerra V, Deschoemaeker S, Bruyere F, Wenes M, Hamm A, Serneels J, Magat J, Bhattacharyya T, Anisimov A, Jordan BF, Alitalo K, Maxwell P, Gallez B, Zhuang ZW, Saito Y, Simons M, De Palma M, Mazzone M, Macrophage skewing by Phd2 haplodeficiency prevents ischaemia by inducing arteriogenesis, Nature 479 (7371) (2011) 122–126. [PubMed: 21983962]

[47]. Mantovani A, Sozzani S, Locati M, Allavena P, Sica A, Macrophage polarization: tumor-associated macrophages as a paradigm for polarized M2 mononuclear phagocytes, Trends Immunol. 23 (11) (2002) 549–555. [PubMed: 12401408]

[48]. Jetten N, Verbruggen S, Gijbels MJ, Post MJ, De Winther MP, Donners MM, Anti-inflammatory M2, but not pro-inflammatory M1 macrophages promote angiogenesis in vivo, Angiogenesis 17 (1) (2014) 109–118. [PubMed: 24013945]

[49]. Grunewald M, Avraham I, Dor Y, Bachar-Lustig E, Itin A, Jung S, Chimenti S, Landsman L, Abramovitch R, Keshet E, VEGF-induced adult neovascularization: recruitment, retention, and role of accessory cells, Cell 124 (1) (2006) 175–189. [PubMed: 16413490]

[50]. Hamm A, Veschini L, Takeda Y, Costa S, Delamarre E, Squadrito ML, Henze AT, Wenes M, Serneels J, Pucci F, Roncal C, Anisimov A, Alitalo K, De Palma M, Mazzone M, PHD2 regulates arteriogenic macrophages through TIE2 signalling, EMBO Mol. Med 5 (6) (2013) 843–857.

[51]. Fung E, Helisch A, Macrophages in collateral arteriogenesis, Front. Physiol 3 (2012) 353. [PubMed: 23055975]

[52]. Bruce AC, Kelly-Goss MR, Heuslein JL, Meisner JK, Price RJ, Peirce SM, Monocytes are recruited from venules during arteriogenesis in the murine spinotrapezius ligation model, Arterioscler. Thromb. Vasc. Biol 34 (9) (2014) 2012–2022. [PubMed: 24969773]

[53]. Christoffersson G, Vagesjo E, Vandooren J, Liden M, Massena S, Reinert RB, Brissova M, Powers AC, Opdenakker G, Phillipson M, VEGF-A recruits a proangiogenic MMP-9-delivering neutrophil subset that induces angiogenesis in transplanted hypoxic tissue, Blood 120 (23) (2012) 4653–4662. [PubMed: 22966168]

[54]. Bergmann CE, Hoefer IE, Meder B, Roth H, van Royen N, Breit SM, Jost MM, Aharinejad S, Hartmann S, Buschmann IR, Arteriogenesis depends on circulating monocytes and macrophage accumulation and is severely depressed in op/op mice, J. Leukoc. Biol 80 (1) (2006) 59–65. [PubMed: 16684892]

[55]. Awojoodu AO, Ogle ME, Sefcik LS, Bowers DT, Martin K, Brayman KL, Lynch KR, Peirce-Cottler SM, Botchwey E, Sphingosine 1-phosphate receptor 3 regulates recruitment of anti-inflammatory monocytes to microvessels during implant arteriogenesis, Proc. Natl. Acad. Sci. Unit. States Am 110 (34) (2013) 13785.

[56]. Huang C, Das A, Barker D, Tholpady S, Wang T, Cui Q, Ogle R, Botchwey E, Local delivery of FTY720 accelerates cranial allograft incorporation and bone formation, Cell Tissue Res. 347 (3) (2012) 553–566. [PubMed: 21863314]

[57]. Spiller KL, Anfang RR, Spiller KJ, Ng J, Nakazawa KR, Daulton JW, Vunjak-Novakovic G, The role of macrophage phenotype in vascularization of tissue engineering scaffolds, Biomaterials 35 (15) (2014) 4477–4488. [PubMed: 24589361]

[58]. Daley JM, Brancato SK, Thomay AA, Reichner JS, Albina JE, The phenotype of murine wound macrophages, J. Leukoc. Biol 87 (1) (2010) 59–67. [PubMed: 20052800]

[59]. Sindrilaru A, Peters T, Wieschalka S, Baican C, Baican A, Peter H, Hainzl A, Schatz S, Qi Y, Schlecht A, Weiss JM, Wlaschek M, Sunderkotter C, Scharffetter-Kochanek K, An unrestrained proinflammatory M1 macrophage population induced by iron impairs wound healing in humans and mice, J. Clin. Invest 121 (3) (2011) 985–997. [PubMed: 21317534]

[60]. Spiller KL, Nassiri S, Witherel CE, Anfang RR, Ng J, Nakazawa KR, Yu T, Vunjak-Novakovic G, Sequential delivery of immunomodulatory cytokines to facilitate the M1-to-M2 transition of macrophages and enhance vascularization of bone scaffolds, Biomaterials 37 (2015) 194–207. [PubMed: 25453950]

[61]. Spiller KL, Wrona EA, Romero-Torres S, Pallotta I, Graney PL, Witherel CE, Panicker LM, Feldman RA, Urbanska AM, Santambrogio L, Vunjak- Novakovic G, Freytes DO, Differential gene expression in human, murine, and cell line-derived macrophages upon polarization, Exp. Cell Res (2015).

[62]. Qiu P, Inferring phenotypic properties from single-cell characteristics, PloS One 7 (5) (2012), e37038.

[63]. Qiu P, Computational prediction of manually gated rare cells in flow cytometry data, Cytometry 87 (7) (2015) 594–602. [PubMed: 25755118]

[64]. Qiu P, Toward deterministic and semiautomated SPADE analysis, Cytometry 91 (3) (2017) 281–289. [PubMed: 28234411]

[65]. Murray PJ, Allen JE, Biswas SK, Fisher EA, Gilroy DW, Goerdt S, Gordon S, Hamilton JA, Ivashkiv LB, Lawrence T, Locati M, Mantovani A, Martinez FO, Mege JL, Mosser DM, Natoli G, Saeij JP, Schultze JL, Shirey KA, Sica A, Suttles J, Udalova I, van Ginderachter JA, Vogel SN, Wynn TA, Macrophage activation and polarization: nomenclature and experimental guidelines, Immunity 41 (1) (2014) 14–20. [PubMed: 25035950]

[66]. Knipper JA, Willenborg S, Brinckmann J, Bloch W, Maass T, Wagener R, Krieg T, Sutherland T, Munitz A, Rothenberg ME, Niehoff A, Richardson R, Hammerschmidt M, Allen JE, Eming SA, Interleukin-4 receptor alpha signaling in myeloid cells controls collagen fibril assembly in skin repair, Immunity 43 (4) (2015) 803–816. [PubMed: 26474656]

[67]. Choo EH, Lee JH, Park EH, Park HE, Jung NC, Kim TH, Koh YS, Kim E, Seung KB, Park C, Hong KS, Kang K, Song JY, Seo HG, Lim DS, Chang K, Infarcted myocardium-primed dendritic cells improve remodeling and cardiac function after myocardial infarction by modulating the regulatory T cell and macrophage polarization, Circulation 135 (15) (2017) 1444–1457. [PubMed: 28174192]

[68]. Noble A, Giorgini A, Leggat JA, Cytokine-induced IL-10-secreting CD8 T cells represent a phenotypically distinct suppressor T-cell lineage, Blood 107 (11) (2006) 4475–4483. [PubMed: 16467201]

[69]. James E, Scott D, Chai JG, Millrain M, Chandler P, Simpson E, HY peptides modulate transplantation responses to skin allografts, Int. Immunol 14 (11) (2002) 1333–1342. [PubMed: 12407024]

[70]. Florquin S, Amraoui Z, Goldman M, T cells made deficient in interleukin-2 production by exposure to staphylococcal enterotoxin B in vivo are primed for interferon-gamma and interleukin-10 secretion, Eur. J. Immunol 25 (5) (1995) 1148–1153. [PubMed: 7774618]
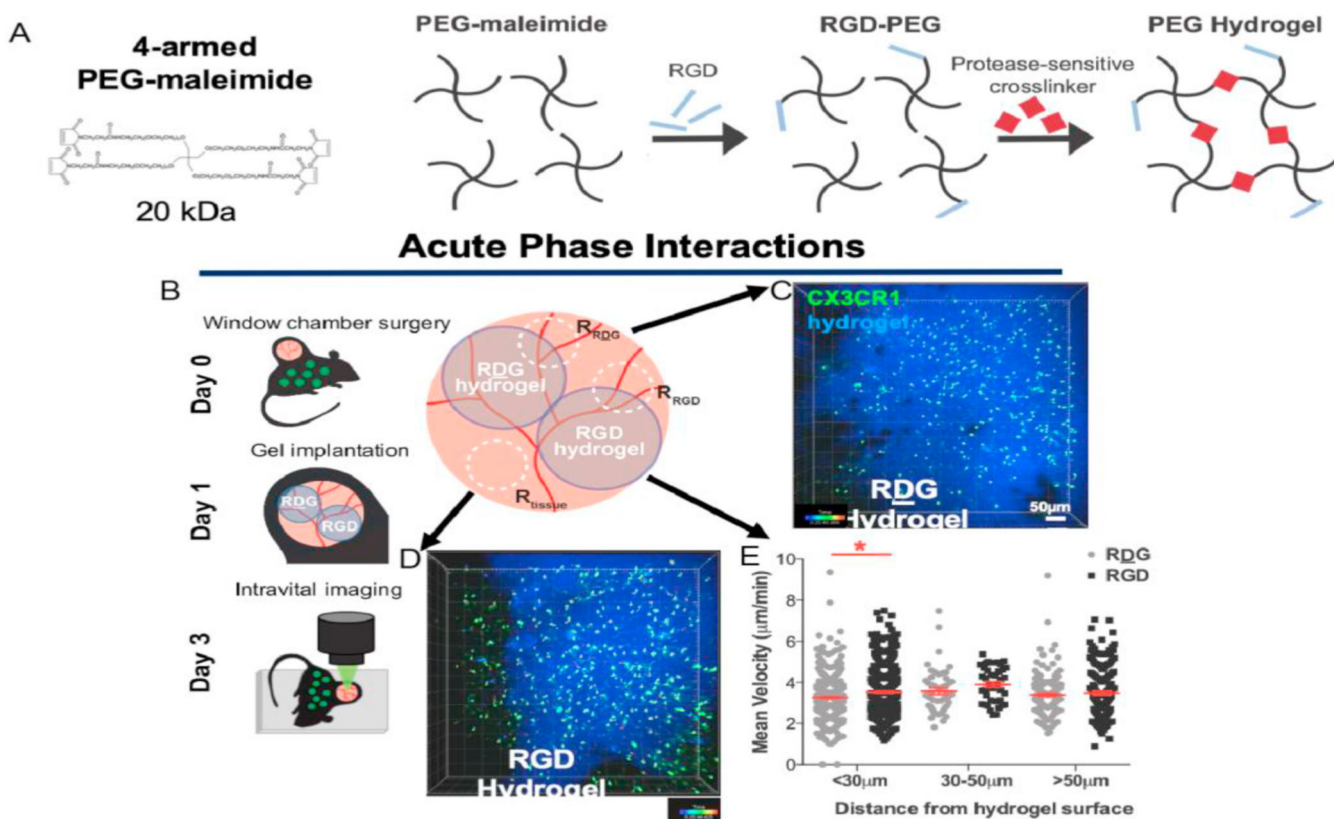
Fig. 1.

Protease-degradable PEG hydrogels functionalized with RGD recruit immune cells. (A) 4-arm PEG maleimide macromers were functionalized with RGD peptides and crosslinked with a protease sensitive crosslinker (VPM) to form a hydrogel. (B) Dorsal skinfold window chambers were performed in in CX3CR1gfp/+ mice. One RDG- (C) and one RGD-functionalized (D) hydrogel were placed on the exposed layer at day 1. At day 3, intravital confocal microscopy was performed. Z-stacks were acquired in each region. CX3CR1+ cells are shown in green, fluorescently tagged hydrogel is shown in blue. Scale bar, 100 μm. (D) Mean velocity of CX3CR1+ cells, classified by their minimum distance from the hydrogel surface. *p < 0.05 compared to RDG hydrogel by Kruskal-Wallis. n = 3 mice. (For interpretation of the references to color in this figure legend, the reader is referred to the Web version of this article.)
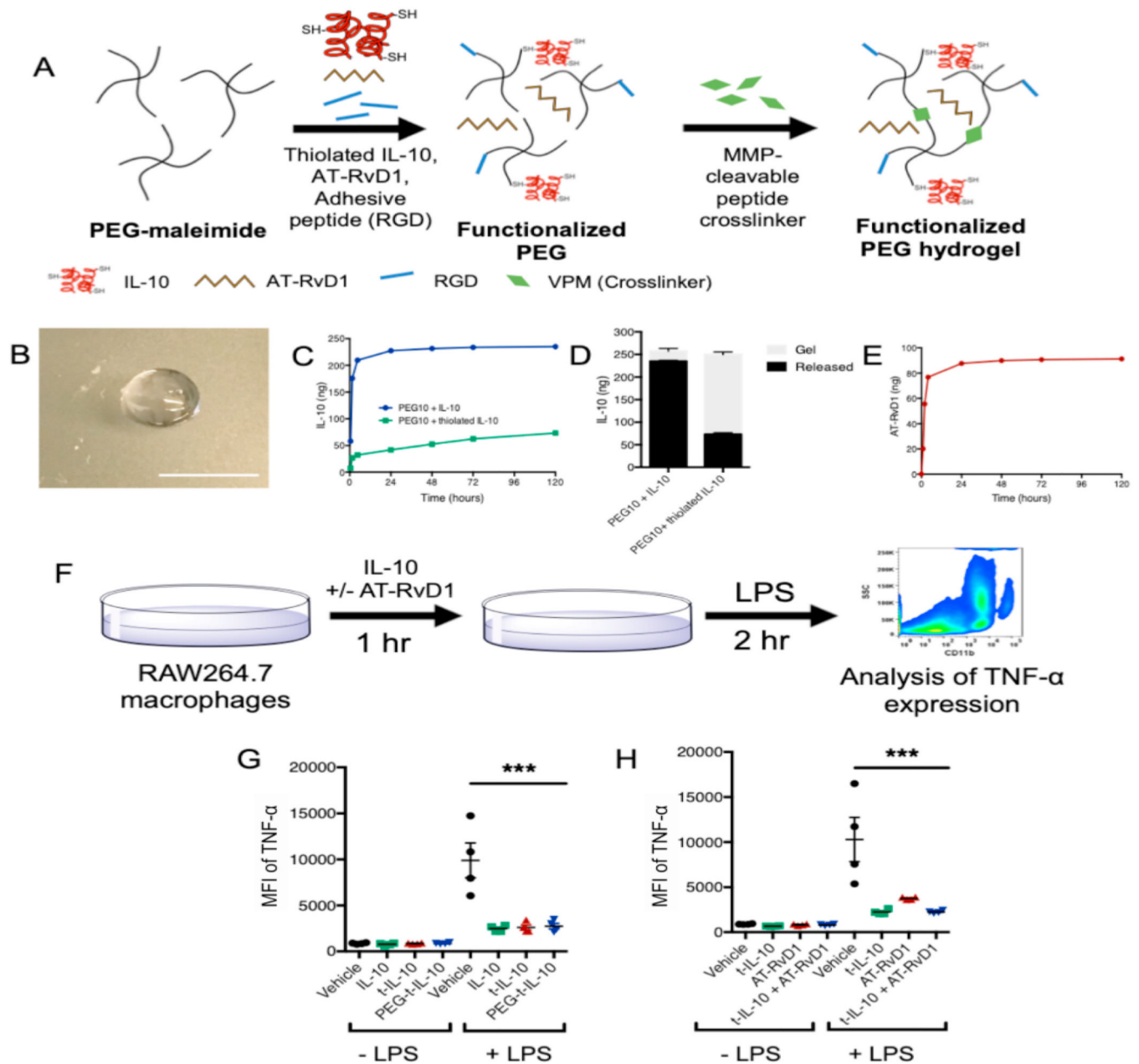
**Fig. 2. Hydrogel schematics, release profiles, and bioactivity.**

(A)Hydrogel fabrication method (B) Resultant macroscopic image of preformed hydrogels (C) Release of unthiolated and thiolated IL-10 from 20kDA PEG-MAL hydrogels over the course of 5 days (D) Amount of IL-10 or thiolated IL-10 remaining in the gels at the end of the release study. (E) Release of AT-RvD1 from 20kDA PEG-MAL hydrogels over the course of 5 days. (F) Schematic of bioactivity assay. (G) Bioactivity of IL-10 following thiolation and PEG conjugation (H) Bioactivity of AT-RvD1 and IL-10 combinations. Statistical analysis was performed using one-way ANOVA with Tukey's post-hoc test, ***p > 0.001, n = 4. AT-RvD1 alone and dual IL-10+AT-RvD1 increase vascular remodeling.
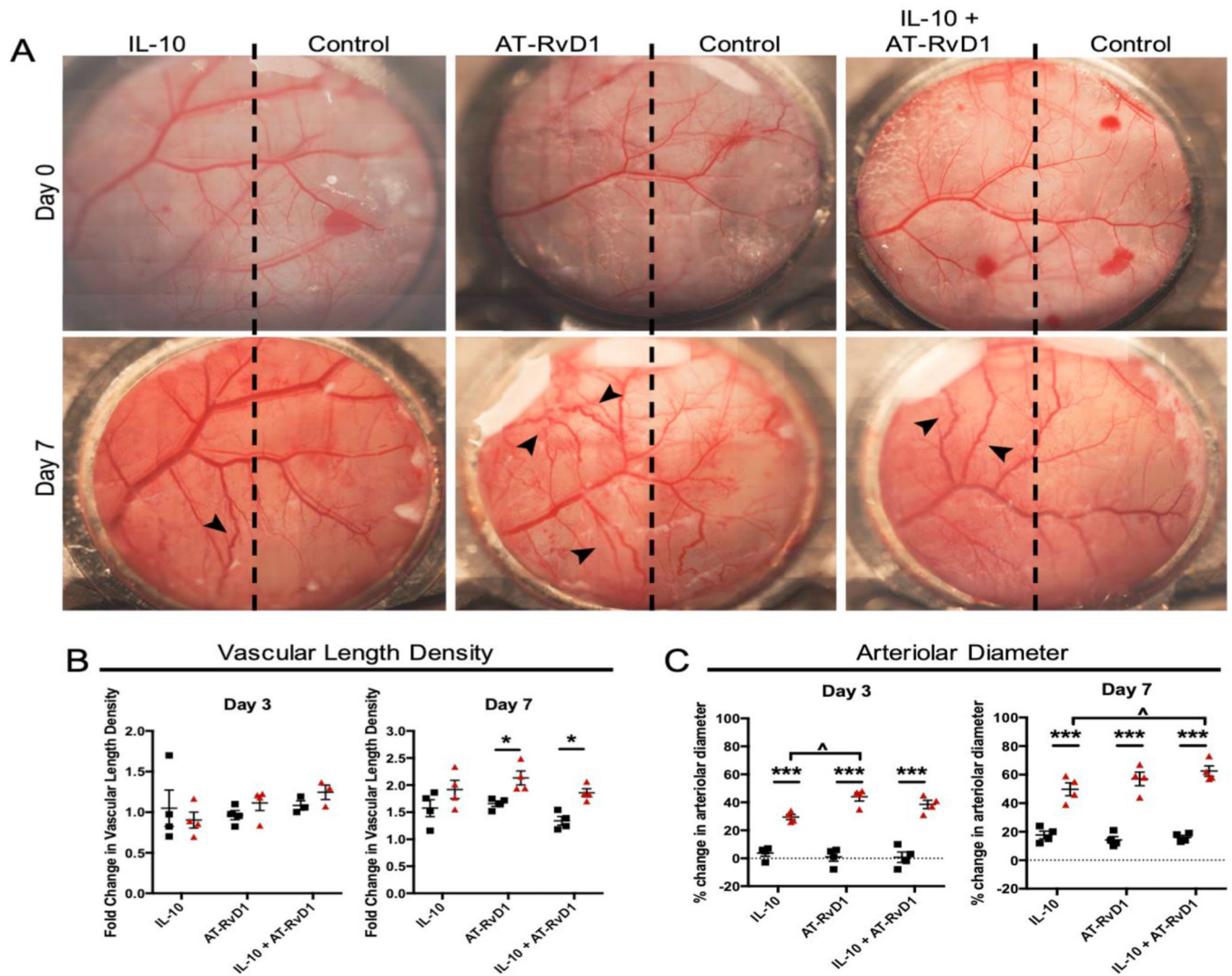
Fig. 3. Vascular remodeling following immunomodulatory hydrogel injection.
(A) Brightfield micrographs of dorsal tissue at day 0 and at day 7 following treatment with immunomodulatory PEG-MAL hydrogels. Quantification of the vascular metrics (B) length density and (C) arteriolar diameter. Data presented as mean ± S.E.M. Statistical analyses were performed two-way repeated measures ANOVA with Tukey's and Bonferroni post hoc tests. *$p < 0.05$, **$p < 0.01$, ***$p < 0.001$ compared to internal control, ^$p < 0.05$ compared to treatment group. n = 4 animals per group. Scale bars, 1 mm.
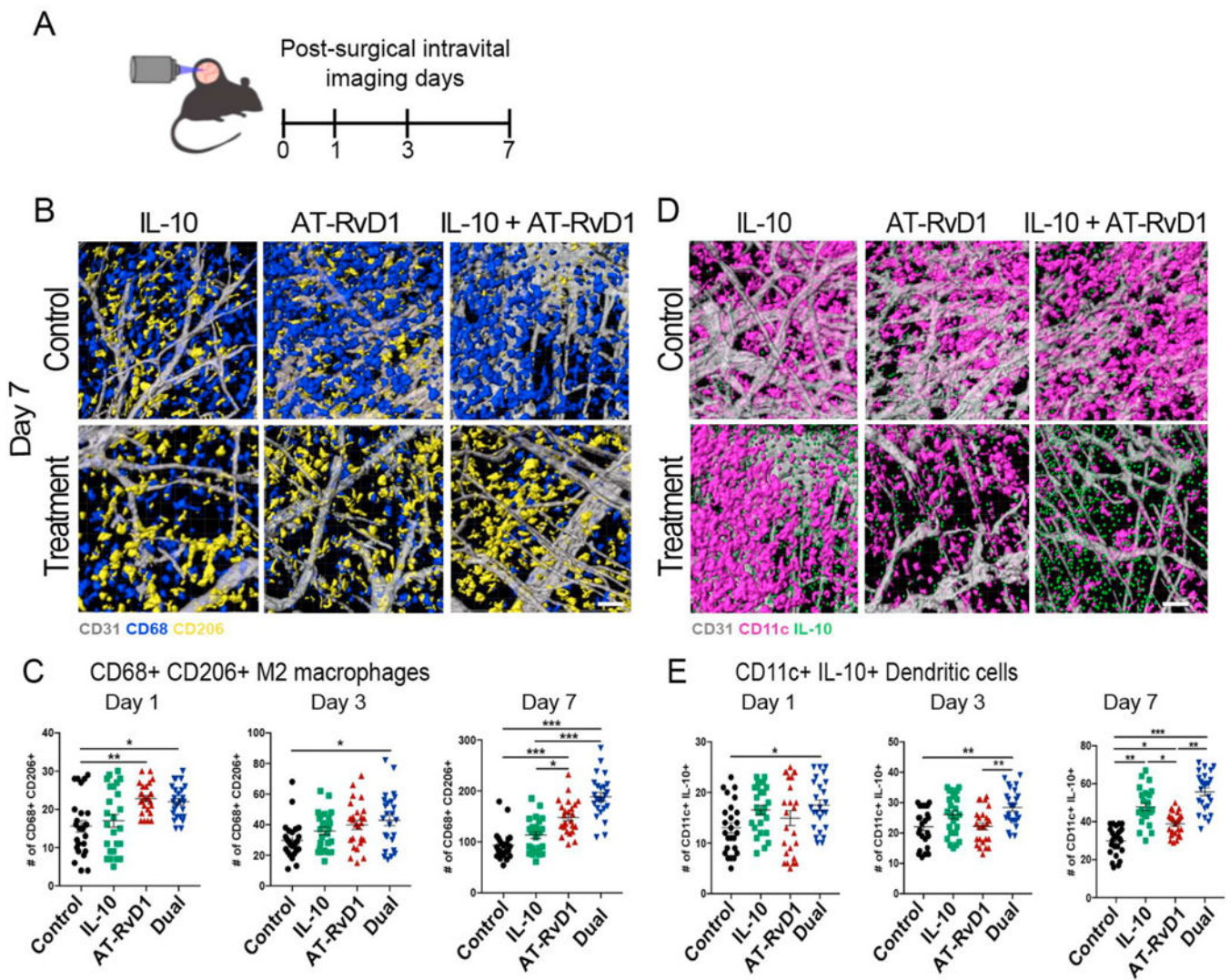
Fig. 4. 3D analysis of M2 and IL-10þ DCs in dorsal tissue.

(A) Intravital imaging was performed on immunomodulatory hydrogels implanted into the murine DSWC model. (B) Imaris renderings of CD68^{+} macrophage and CD206+ M2 macrophage accumulation by day 7. (C) Quantification of total CD68^{+} CD206+ double positive cells found in Imaris renderings from day 1 to day 7. (D) Imaris renderings of CD11c + dendritic cell and IL-10 staining over time. (E) Quantification of total CD11^{+} IL-10+ double positive cells found in Imaris renderings from day 1 to day 7. Scale bars, 30 μm. Data presented as mean ± S.E.M. Statistical analyses were performed using Mann-Whitney Test *p < 0.05, **p < 0.01 ***p < 0.001 compared to control by Kruskal-Wallis, n > 100 cells, across 3–4 animals per group.
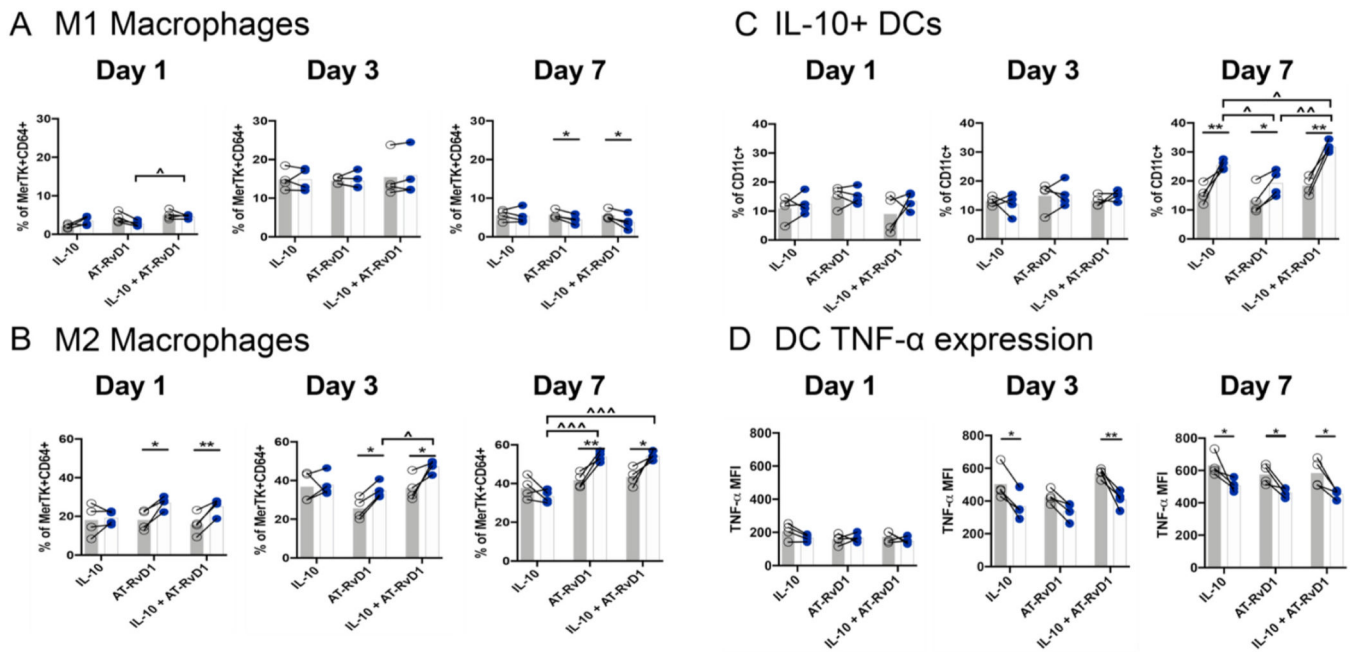
Fig. 5. Anti-inflammatory macrophages and dendritic cells accumulate after local immunomodulatory hydrogel delivery.

Flow cytometric analysis of macrophages, (A) CD86^{+} M1 Macrophage and (B) CD206+ M2 macrophage populations, and dendritic cells, IL-10 (C) and TNF-α (D) expression in the dorsal skinfold window chamber following treatment with immunomodulatory PEG-MAL Hydrogels. Open circles correspond to unloaded internal control; closed circles are treated tissue. Statistical analysis was performed using two-way repeated measures ANOVA with Tukey's or Bonferroni post-hoc test. Data presented as internal control and treatment with connecting lines. *p < 0.05, **p < 0.01 compared to internal control, ^p < 0.05, ^^p < 0.01, ^^^p < 0.001 compared to other treatment group, n = 4. Dimensionality reduction analysis reveals trends in innate immune cell heterogeneity by day 7.
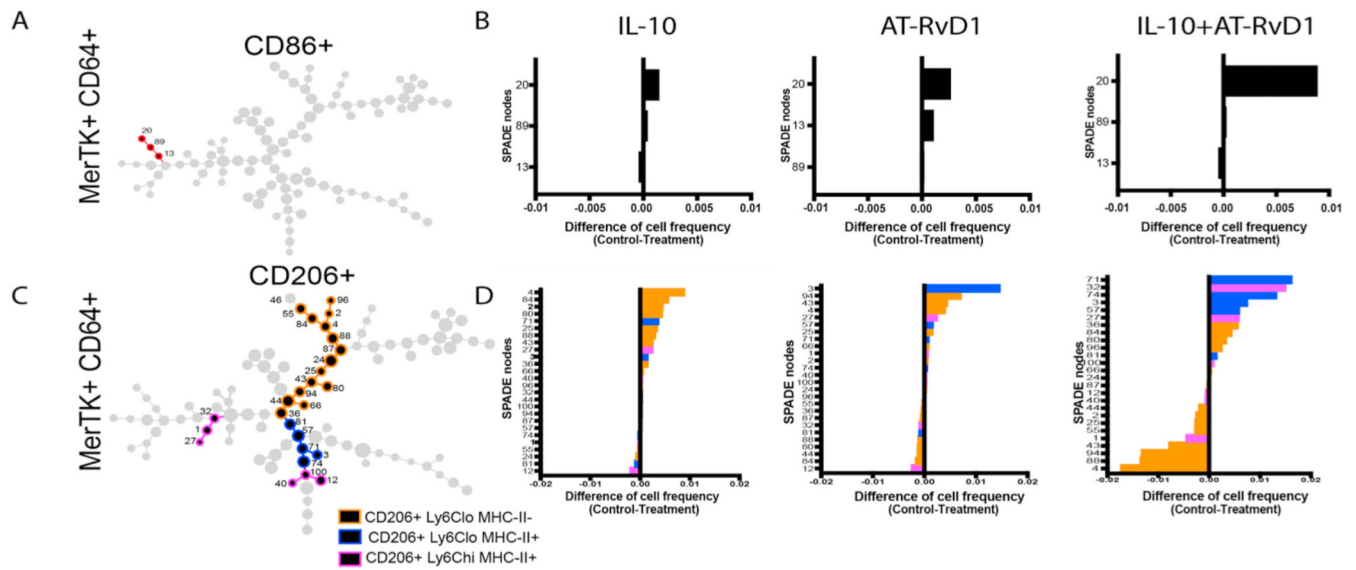
Fig. 6.
Innate immune response to immunomodulatory hydrogels. SPADE trees were developed following flow cytometric analysis to identify cell subsets. Macrophage trees were developed after gating for CD11b + MerTK + CD64$^+$ cells. SPADE analysis indicates nodes positive for CD86$^+$ M1 macrophages (A) and CD206+ M2 macrophages (C) and tornado plots were used to identify shifts in cell frequency after IL-10 alone, AT-RvD1 alone, and dual delivery (B, D). SPADE analysis reveals trends towards unexpected pro-regenerative adaptive immune cell population at day 7 following dual treatment with IL-10+AT-RvD1.
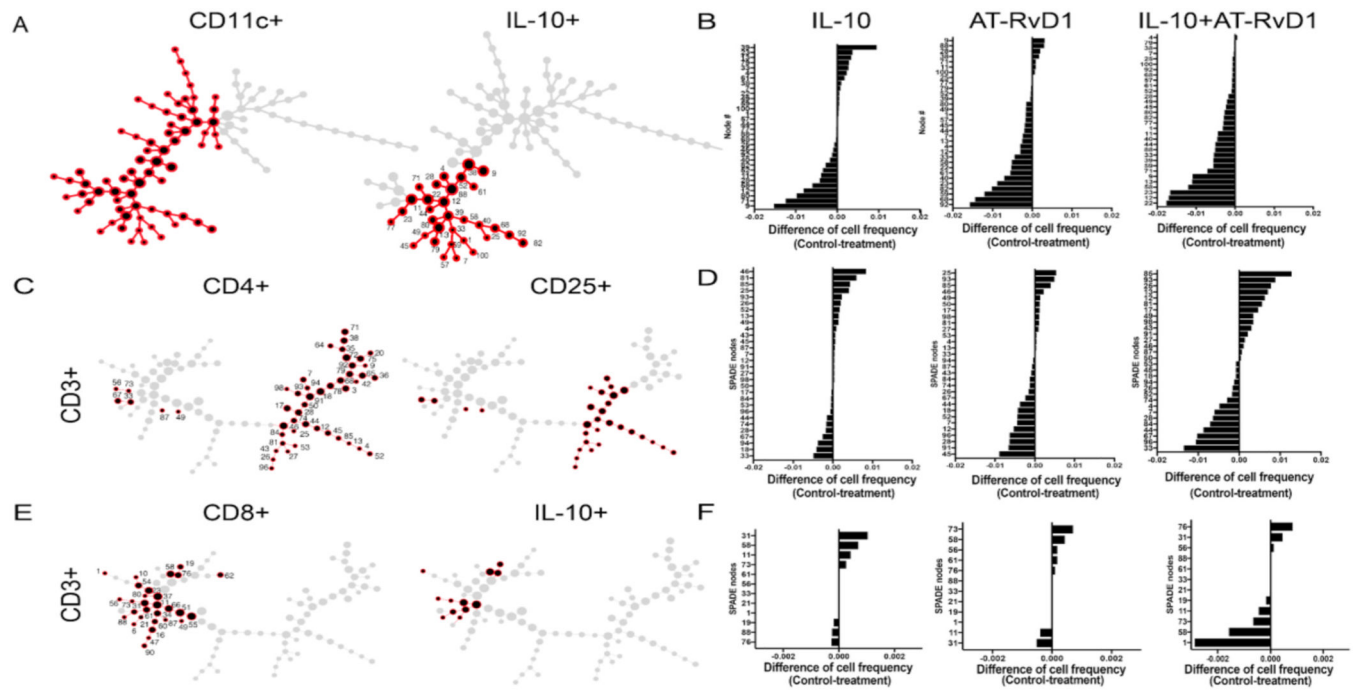
Fig. 7.
DC and adaptive immune response to immunomodulatory hydrogels. SPADE trees were
developed following flow cytometric analysis to identify cell subsets. (A) SPADE was used
to create a CD11c + tree to identify DCs, which was further analyzed to identify nodes that
indicate L-10+ DCs. (B) Individual node cell frequency distributions in each treatment group
were analyzed using tornado plots. (C) CD3^{+} base trees were developed after gating for
CD3^{+} cells SPADE trees show nodes positive for CD4^{+} CD25^{+} T-cells. (D) Tornado plots
were utilized to identify shifts in cell frequency after IL-10 alone, AT-RvD1 alone, and dual
delivery (E). SPADE was used to create a CD8^{+} tree to identify cytotoxic T-cells, which was
further analyzed to identify nodes that were positive for intracellular IL-10. (F) Individual
node cell frequency distributions in each treatment group were analyzed using tornado plots.